nature astronomy

ARTICLES

https://doi.org/10.1038/s41550-022-01754-4

Check for updates

Snapshot of a magnetohydrodynamic disk wind traced by water maser observations

Luca Moscadelli[1]✉, Alberto Sanna[2,3], Henrik Beuther[4], André Oliva[5,6] and Rolf Kuiper[7]

The formation of astrophysical objects of different nature, from black holes to gaseous giant planets, involves a disk–jet system, where the disk drives the mass accretion onto a central compact object and the jet is a fast collimated ejection along the disk rotation axis. Magnetohydrodynamic disk winds can provide the link between mass accretion and ejection, which is essential to ensure that the excess angular momentum is removed and accretion can proceed. However, until now, we have been lacking direct observational proof of disk winds. Here we present a direct view of the velocity field of a disk wind around a forming massive star. Achieving a very high spatial resolution of about 0.05 au, our water maser observations trace the velocities of individual streamlines emerging from the disk orbiting the forming star. We find that, at low elevation above the disk midplane, the flow co-rotates with its launch point in the disk, in agreement with magneto-centrifugal acceleration. Beyond the co-rotation point, the flow rises spiralling around the disk rotation axis along a helical magnetic field. We have performed (resistive-radiative-gravito-)magnetohydrodynamic simulations of the formation of a massive star and record the development of a magneto-centrifugally launched jet presenting many properties in agreement with our observations.

Magnetohydrodynamic (MHD) disk winds have been proposed to be the engines of the powerful jets observed at varying length scales in many diverse sources, from young stellar objects[1] (YSOs) to black holes[2]. According to the classical model of an ideal MHD disk wind[2], in the reference frame co-rotating with the launch point, the flow streams along the magnetic-field line anchored to the accretion disk. An observer at rest sees magneto-centrifugal acceleration: the magnetic field keeps the flow in co-rotation with its launch point while its radial distance increases, until reaching the Alfvén point where the poloidal kinetic and magnetic energies are equal. Beyond the Alfvén point, the flow spirals outwards along the rotation axis with a stably increasing ratio of the streaming onto the rotational velocity, until it gets eventually collimated into a fast jet[3,4]. So far, the best observational evidence for an MHD disk wind has been the finding of line-of-sight velocity gradients transversal to the jet axis, which are interpreted in terms of jet rotation and the imprint of the magneto-centrifugal acceleration[5–8]. However, this is indirect evidence, and the derivation of key parameters, such as the launch radius and the magnetic lever arm, can be seriously affected by systematic biases[9]. On scales of ~100 au, a few studies based on very long baseline interferometry (VLBI) maser observations have revealed rotating disk-like[10–12], conical[13] or cylindrical[14] maser distributions at the jet root, but the streamlines of a disk wind have been never traced, until now.

IRAS 21078+5211 is a star-forming region of high bolometric luminosity, $5\times10^3\,L_\odot$ (ref. [15]) at a distance of 1.63 ± 0.05 kpc (ref. [16]), and harbours a cluster of forming massive stars. On scales of a few 100 au, by employing the Northern Extended Millimeter Array (NOEMA), a disk[17] is observed in high-density molecular tracers (CH_3CN and HC_3N; Fig. 1a) rotating around a YSO of mass $5.6\pm2\,M_\odot$. Interferometric observations at radio wavelengths (5 cm) using the Jansky Very Large Array (JVLA) have revealed a jet[15] directed northeast–southwest (position angle from north to east, PA ≈ 44°) emerging from the YSO, whose position at the centre of the disk is pinpointed by compact thermal emission observed with the JVLA at 1.3 cm. During 2010–2011, we have performed multi-epoch Very Long Baseline Array (VLBA) observations of the maser emission of the water molecule at 22 GHz. These observations have discovered a cluster of masers placed ~100 au northeast from the YSO, whose proper motions are collimated northeast–southwest (PA = 49°) and trace the base of the jet from the YSO[15] (Fig. 1b). The analysis of the three-dimensional (3D) maser motions, specifically the local standard of rest (LSR) velocity (V_{LSR}) gradient transversal to the jet axis and the constant ratio between the toroidal and poloidal velocities, suggested that the jet could be launched from an MHD disk wind.

In October 2020, we performed novel observations (Fig. 2a) of the water maser emission in IRAS 21078+5211 by including all telescopes available in the VLBI network, with the aim to simulate next-generation radio interferometers that will improve current sensitivities by more than an order of magnitude (see 'Observations' in Methods). In the following, we show that these observations prove that the water masers trace magnetized streams of gas emerging from the YSO's disk (see Fig. 2b and 'Simulation snapshot of a forming massive star' in Methods). The maser emission concentrates in three regions to the northeast, north and southwest, inside the three dotted rectangles of Fig. 2a. Along the jet axis (the dashed red line in Fig. 2a), whose sky projection is known from previous observations of the maser proper motions and radio jet (see 'Shock type and corresponding flow kinematics of water masers' in Methods), we observe two elongated structures, blue- and redshifted (with respect to the systemic V_{LSR} of the YSO: $V_{sys} = -6.4$ km s^{-1}) to northeast and southwest, respectively. These structures are the opposite lobes of a collimated outflow from the YSO, located in between the two lobes;

[1]Osservatorio Astrofisico di Arcetri, Istituto Nazionale di Astrofisica, Firenze, Italy. [2]Osservatorio Astronomico di Cagliari, Istituto Nazionale di Astrofisica, Selargius, Italy. [3]Max-Planck-Institut für Radioastronomie, Max Planck Gesellschaft, Bonn, Germany. [4]Max Planck Institute for Astronomy, Max Planck Gesellschaft, Heidelberg, Germany. [5]Institut für Astronomie und Astrophysik, Universität Tübingen, Tübingen, Germany. [6]Space Research Center (CINESPA), School of Physics, University of Costa Rica, San José, Costa Rica. [7]Faculty of Physics, University of Duisburg-Essen, Duisburg, Germany. ✉e-mail: luca.moscadelli@inaf.it

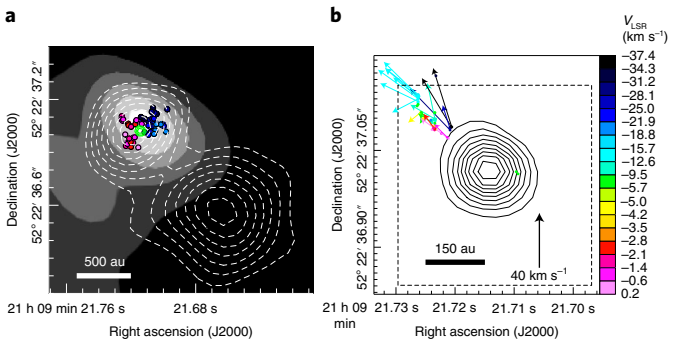

Fig. 1 | Previous NOEMA, JVLA and VLBA observations towards IRAS 21078+5211. a, The greyscale (from 10 mJy per beam to 35 mJy per beam) map reproduces the NOEMA 1.37 mm continuum emission[17]. The coloured dots represent the channel emission peaks of the CH_3CN $J_K = 12_K$–11_K ($K = 3$–6) and HC_3N $J = 24$–23 lines (where J and K are the quantum numbers of the molecular rotational transition), with colours denoting the channel V_{LSR}: blue for [−13.6, −10] km s^{-1} and red [−2.5, 0.5] km s^{-1}. The green (70%, 80% and 90% of 0.50 mJy per beam) and white (from 30% to 90%, in steps of 10% of 0.096 mJy per beam) contours show the JVLA A-Array continuum at 1.3 cm and 5 cm, respectively. **b**, Coloured dots and arrows give absolute positions and proper motions of the 22 GHz water masers determined with multi-epoch (2010–2011) VLBA observations[15], with colours denoting the maser V_{LSR}. The black contours (from 10% to 90%, in steps of 10% of 0.50 mJy per beam) indicate the JVLA A-Array continuum at 1.3 cm. The dashed rectangle delimits the field of view plotted in Fig. 2a.

the disk axis (the black dashed line in Fig. 2a) is the intercept of the jet axis at the YSO position. From previous VLBA observations, we know that the jet axis has to lay close to the plane of the sky, with an inclination of ≤30°. According to the maser V_{LSR}, the jet is inclined towards us to the northeast, and away from us to the southwest.

The jet and disk axes provide a convenient coordinate system to refer the maser positions to. In the following, we present the interpretation of the maser kinematics, which is based on the analysis of the three independent observables: z, the elevation above the disk plane (or offset along the jet), R, the radial distance from the jet axis (or transversal offset), and the maser V_{LSR}. As discussed in 'Observations' in Methods, the accuracy of the maser positions is ~0.05 au, and that of the maser $V_{LSR} \approx 0.5$ km s^{-1}. Without loss of generality, we can express the maser velocities as the sum of two terms, one associated with the toroidal component or rotation around the jet axis, V_{rot}, and the other associated with the poloidal component including all the contributions owing to non-rotation, V_{off}. As the jet axis is close to the plane of the sky and we observe the rotation close to edge-on (Fig. 3), we can write:

$$V_{LSR} = V_{off} + V_{rot} = V_{off} + \omega \Re \sin(\phi) \quad (1)$$

$$R = \Re \sin(\phi) \quad (2)$$

$$\phi = \omega t \quad (3)$$

where ϕ is the angle between the rotation radius $\Re$ and the line of sight, and ω and t are the angular velocity and the time, respectively.

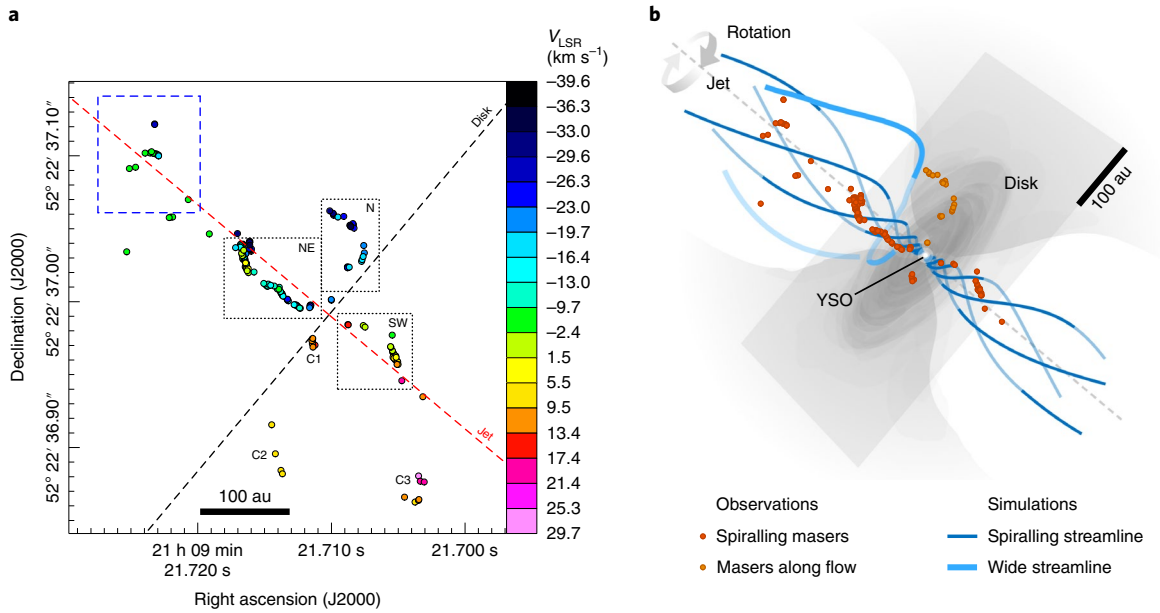

Fig. 2 | Global VLBI observations of the 22 GHz water masers and 3D view of the proposed kinematical interpretation. a, Coloured dots give absolute positions of the 22 GHz water masers, with colours denoting the maser V_{LSR}. The black dotted rectangles encompass the three regions, to the north (N), northeast (NE) and southwest (SW), where maser emission concentrates. The blue dashed rectangle delimits the area of maser emission in the previous VLBA observations, and three distinct maser clusters south of the YSO are labelled C1, C2 and C3 (see 'Kinematics of the water masers further to northeast and south' in Methods). The red and black dashed lines mark the sky-projected jet and disk axis, respectively. **b**, Observed maser positions (red and orange dots) overlaid on streamlines (blue lines) computed from resistive-radiative-gravito-MHD simulations of a jet around a forming massive star (see 'Simulation snapshot of a forming massive star' in Methods). The streamlines close to the rotation axis show significant spiralling motion, in agreement with the kinematic signature of the masers observed in the northeast and southwest regions. The wide streamline from the simulation illustrates the outflowing trajectory of material from the outer disk, similar to the observed masers in the north region. For context, the protostar, the disk and the outflow cavity have been sketched in grey, based on the density structure obtained in the simulations (Supplementary Fig. 1).

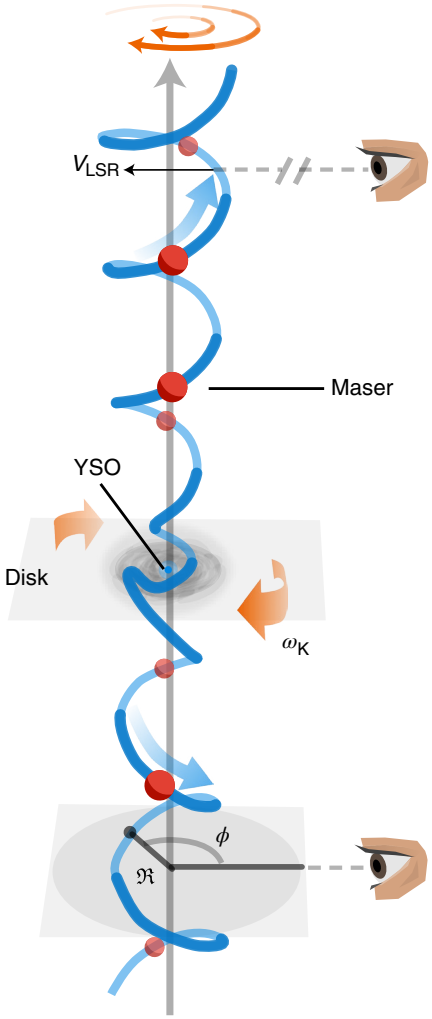

Fig. 3 | The geometry of the spiral motion. Illustration of the spiral motion of the masers (small red balls) along a magnetic-field line (blue) emerging from the YSO's disk. The rotation angle, ϕ, and radius, $\mathfrak{R}$, are labelled. The field line is anchored to a point of the disk rotating at an angular velocity ω_K. This plot is based on the data from (resistive-radiative-gravito-) MHD simulations of a jet around a forming massive star (see 'Simulation snapshot of a forming massive star' in Methods).

Figure 4c shows the remarkable finding that the spatial coordinates z and R of the maser emission in the southwest flow satisfy the relation:

$$R = C\,\sin(f_z(z - z_0)) \tag{4}$$

where C, the amplitude of the sinusoid, f_z, the spatial frequency, and z_0, the position of zero phase, are fitted constants (Table 1). In 'Resolving the northeast emission into three distinct streams' in Supplementary Information, we demonstrate that the masers in the northeast flow can be separated in three different streams (NE-1, NE-2 and NE-3), each of them satisfying the relation (4) (Fig. 5c and Table 1). The comparison of equations (2) and (4) leads to a straightforward interpretation of the sinusoidal relation between the coordinates by taking: (1) $\mathfrak{R} = C$, and (2) $\phi = f_z\,\|z - z_0\|$. The first equation indicates that the rotation radius is the same for all the masers, and the second equation shows that the motions of rotation around and streaming along the jet axis are locked together, which is the condition for a spiral motion. Denoting with V_z the streaming velocity along the jet axis, we can write $\|z - z_0\| = V_z\,t$ and, by comparing with equation (3), we derive the relation between the rotation and streaming velocities:

$$f_z = \omega / V_z \tag{5}$$

According to equation (5), the observation of a well-defined sinusoidal pattern requires that ω and V_z are directly proportional, or constant. The constancy of V_z implies that V_{off} is also constant, because, if the rotation radius does not change, V_{off} is the projection along the line of sight of V_z. Following equations (1) and (2), the constancy of ω and V_{off} would result into a tight linear correlation between V_{LSR} and transversal offsets R. While a good linear correlation between V_{LSR} and R is observed for the southwest and NE-1 spiral motions (Figs. 4b and 5b, black symbols), the scatter in velocity is considerable for the NE-2 spiral motion (Fig. 5b, red symbols). In 'Velocity scatter' in Methods, we investigate the physical reason for the observation of well-defined sinusoidal patterns despite the presence of a significant velocity scatter. Applying the equations of motions for an axisymmetric MHD flow, we find that the magnetic-field configuration has to be helical over the maser emission region, and the motion along such an helical field line, in the reference frame co-rotating with the launch point, leads to the sinusoidal pattern of maser positions.

We consider now the north region (Fig. 2a) and show that, in this region as well, the maser kinematics is consistent with the predictions for an MHD disk wind. The north masers have a larger separation from the jet axis than the northeast and southwest masers. A few nearby masers show quite different V_{LSR}, which could hint at distinct streams, as observed (Fig. 5a) and discussed (see 'Resolving the northeast emission into three distinct streams' in Supplementary Information) for the northeast flow. In this case, however, only a single stream is reasonably well sampled in position and V_{LSR} with the masers, and we focus our kinematical analysis on that. The spatial distribution of this stream presents an arc-like shape: a subset of maser features draws a line at small angle with the disk axis and another group extends at higher elevations about parallel to the jet axis (Fig. 6a). Figure 6c shows that the maser V_{LSR} increases linearly with R in the range $-95\,\text{au} \lesssim R \lesssim -70\,\text{au}$ up to an elevation $z \approx 60\,\text{au}$. The relatively large separation from the jet axis and radial extent, and the arc-like shape of the maser distribution lead us to think that the north emission is observed close to the plane of the sky. In this case, the maser V_{LSR} should mainly trace rotation, which is also expected to be the dominant velocity component at low elevations above the disk. Then, the good linear correlation between V_{LSR} and R indicates that the masers co-rotate at the same angular velocity, $\omega_N = 0.274 \pm 0.005\,\text{km s}^{-1}\,\text{au}^{-1}$, up to $R \approx -95$ au and $z \approx 60$ au. A simple interpretation is in terms of a magneto-centrifugally accelerated stream of gas emerging from a point of the disk. A disk in Keplerian rotation around an YSO of about $5.6\,M_\odot$ attains an angular velocity equal to ω_N at $R \approx 40$ au. The line drawn by the masers at the lowest elevations intercepts the disk axis close to -40 au (Fig. 6a), as expected if the gas, launched from the disk, first streams approximately along a straight line and then progressively bends up along the jet axis. It is noted that, based on equations (1) and (2), the derivation of ω_N does not depend on the maser geometry. Therefore, the finding that the masers lay along a line intercepting the disk at about -40 au provides an 'a posteriori' test of the assumption that the north emission is observed close to the plane of the sky.

The masers found at elevation $z > 60$ au appear to set aside of the arc-like distribution (Fig. 6a) and their V_{LSR} are significantly more negative and do not follow the linear correlation with the radius (Fig. 6c). A natural interpretation is that the location at $R \approx -95$ au and $z \approx 60$ au is the Alfvén point of the stream, and beyond that the gas is not any longer co-rotating. The lever arm of the stream is $\sim(95\,\text{au})/(40\,\text{au}) = 2.4$, in agreement with the values of

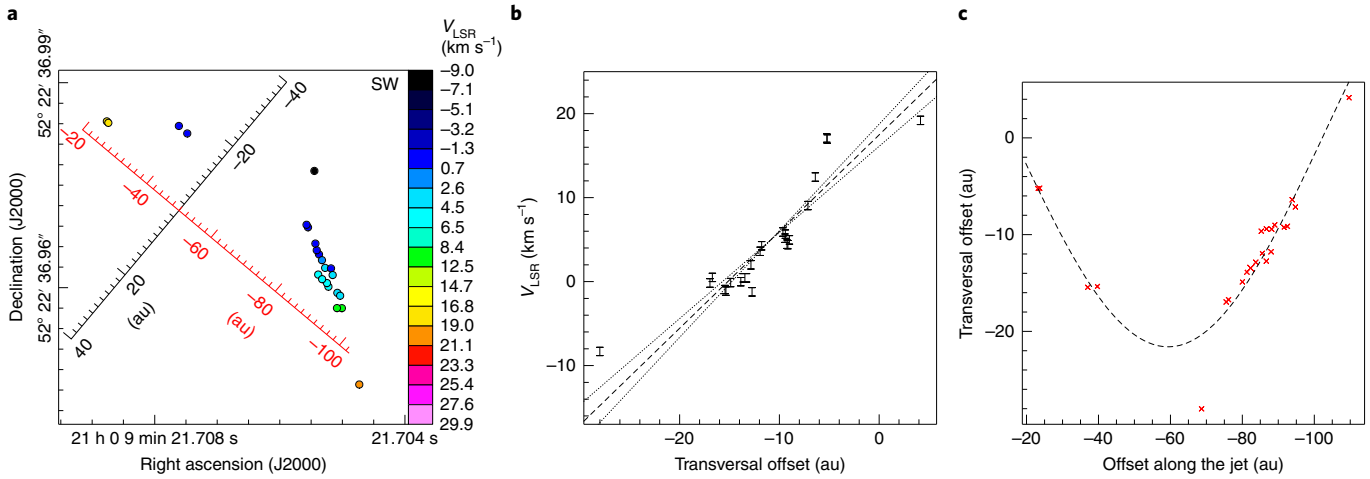

Fig. 4 | The southwest spiral motion. a, Expanding view of the maser positions and V_{LSR} in the southwest region. Coloured dots have the same meaning as in Fig. 2a. The distances along the jet (red) and disk (black) axes are indicated. **b**, Plot of the maser V_{LSR} (and corresponding 2σ errors, denoted with error bars) versus R. The black dashed and dotted lines show the best linear fit and the associated uncertainty, respectively. **c**, Plot of the maser coordinates R versus z. The positional error is smaller than the cross size. The black dashed curve is the fitted sinusoid, whose parameters are reported in Table 1.

Table 1 | Parameters of the linear and sinusoidal fits

	Linear fit		Sinusoidal fit		
Stream	**ω (km s^{-1} au^{-1})**	**V_{off} (km s^{-1})**	**$\mathfrak{R}$ (au)**	**f_z (rad au^{-1})**	**z_0 (au)**
SW	1.15 ± 0.12	17.5 ± 1.3	21.6 ± 1.0	0.0366 ± 0.0012	−16.5 ± 1.9
NE-1	1.15 ± 0.09	−29.2 ± 0.6	36 ± 5	0.0307 ± 0.0008	16.3 ± 2.0
NE-2	0.64 ± 0.27	−10.9 ± 3.0	22.9 ± 0.5	0.0386 ± 0.0008	47.8 ± 1.2
NE-3	2.0 ± 0.5[a]	−49 ± 27	17.2 ± 0.3	0.0405 ± 0.0023	7.3 ± 2.3

Column 1 denotes the maser stream. Columns 2 and 3 provide the values of ω and V_{off} from the linear fit of maser V_{LSR} versus R. Columns 4, 5 and 6 report the amplitude, the spatial frequency and the position of zero phase, respectively, of the sinusoidal fit of the maser coordinates R versus z. [a]The determination of this error, smaller than the value, 1.7 km s^{-1} au^{-1}, from the linear fit, is discussed in 'The angular velocity of the NE-3 stream' in Supplementary Information.

2–3 predicted by theory[18,19]. The more negative V_{LSR} are explained if V_z (and the absolute value of V_{off}) increases with the elevation, as a consequence of the magneto-centrifugal launching. The linear correlation between V_{LSR} and z ($dV_{LSR}/dz = -0.195 \pm 0.002$ km s^{-1} au^{-1}) shown in Fig. 6b results from the combination of the two regimes: (1) sub-Alfvénic, where $V_{LSR} \propto R$ and the gas streams approximately along a straight line, that is, $R \propto z$; and (2) trans-Alfvénic, where V_z increases quickly with z and V_{off} starts to be significant.

From the previous analysis, an MHD disk wind seems to be a natural frame to explain both the spiral motions traced by the masers close to the jet axis in the northeast and southwest regions and the gas co-rotation along the north stream. If some locations of the YSO's disk are perturbed, the flow emerging from those perturbed launch points should harbour internal shocks (see 'Shock type and corresponding flow kinematics of water masers' in Methods), which travel outwards along spiralling trajectories. These internal shocks provide physical conditions suitable for the excitation of the water masers[20–22]. The spiral motions traced with the masers would correspond to portions of the trajectories beyond the Alfvén point where the rotation radius keeps about constant. An essential feature of the proposed model is that, as the launch point rotates, the maser emissions have to travel along spatially distinct, spiralling trajectories. These trajectories are invariant under rotation and nearby masers share the same orbital parameters. However, as the masers sample different trajectories, we need to make a distinction between the angular velocity of the trajectory, ω, derived through the linear fit of the maser V_{LSR} versus R (see equations (1) and (2), and Figs. 4b and 5b), and the effective angular velocity of rotation, ω_e, the one to be used in equations (3) and (5). As the different trajectories are rigidly anchored to the launch point and water masers at higher (absolute) elevations have been launched earlier in time, the simple relation holds:

$$\omega_e = \omega - \omega_K \quad (6)$$

where ω_K is the Keplerian angular velocity of the launch point. Equation (6) shows that ω_e is the angular velocity of the spiralling trajectory as observed in the reference frame co-rotating with the launch point. On the basis of axisymmetric MHD models[9,23], the ratio ω_K/ω increases stably from 1 up to a value ~4 while the gas climbs from z_A to 10 $\mathfrak{R}_K$, where z_A is the elevation of the Alfvén point and $\mathfrak{R}_K$ is the launch radius. Being $\omega \leq \omega_K$, the negative value of ω_e indicates that the rotation angle of the maser positions decreases with z. Following the previous discussion, equation (5) has to be corrected by replacing ω with ω_e:

$$f_z = \| \omega_e \| / V_z \quad (7)$$

A good test of the above considerations comes directly from our data. Assuming that all the masers move along a single trajectory and using the fitted values of ω and f_z in equation (5), we obtain implausibly small values for V_z: 31 km s^{-1}, 37 km s^{-1}, 17 km s^{-1} and 49 km s^{-1}, for the southwest, NE-1, NE-2 and NE-3 spiral motions, respectively. There are two strong observational evidences that

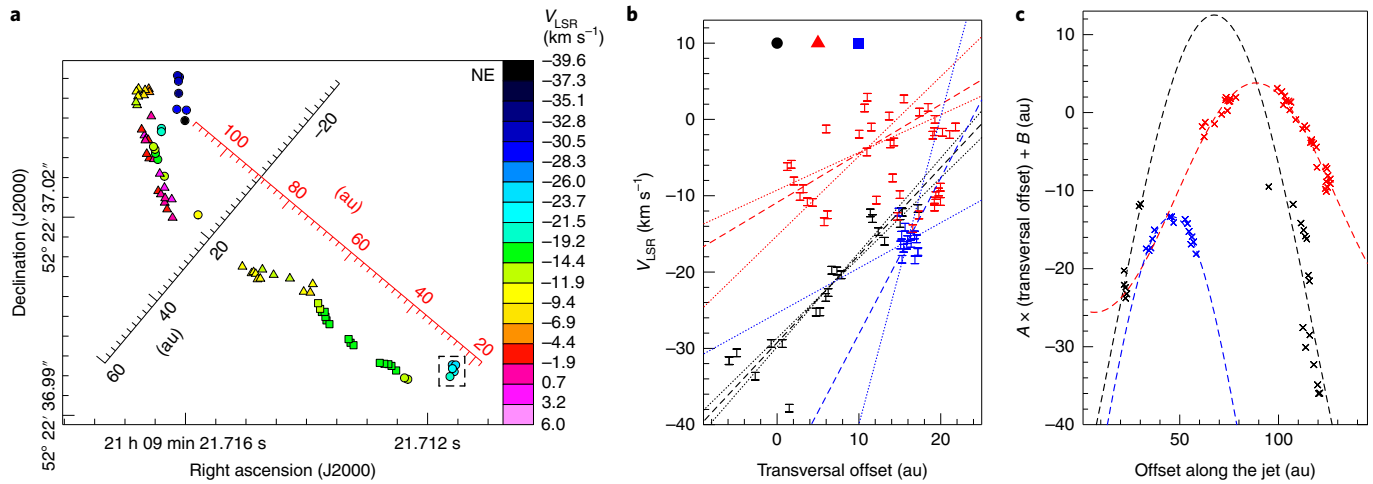

Fig. 5 | The northeast spiral motions. a, Expanding view of the maser positions and V_{LSR} in the northeast region. Different symbols are employed to identify the three spiral motions: dots for the NE-1, triangles for the NE-2 and squares for the NE-3 spiral motion. Colours denote the maser V_{LSR}. The distances along the jet (red) and disk (black) axes are indicated. The black dashed rectangle encompasses the maser cluster closest to the YSO. **b**, In this and the following panel, black, red and blue colours refer to masers belonging to the NE-1, NE-2 and NE-3 streams, respectively. Error bars, dashed lines and dotted lines have the same meaning as in Fig. 4b. Masers in the NE-2 stream with similar radii, 10 au ≤ R ≤ 22 au, but different elevations, 60 au ≤ z < 90 au and z ≥ 90 au, have V_{LSR} different by ~10 km s^{-1} (see 'Velocity scatter' in Methods). For the NE-2 stream, the linear fit of the V_{LSR} has been performed considering only the masers with z ≥ 90 au. **c**, Plot of the linear transformation (using the coefficients A and B) of R versus z. For each of the three streams, the coefficients A and B are taken equal to the corresponding values of ω and V_{off}, respectively, in Table 1. We plot the linear transformation of the radii to reduce the overlap and improve the visibility of each of the three streams. The dashed curves are the fitted sinusoids. In Table 1, we report the parameters of the sinusoidal fits of the radii.

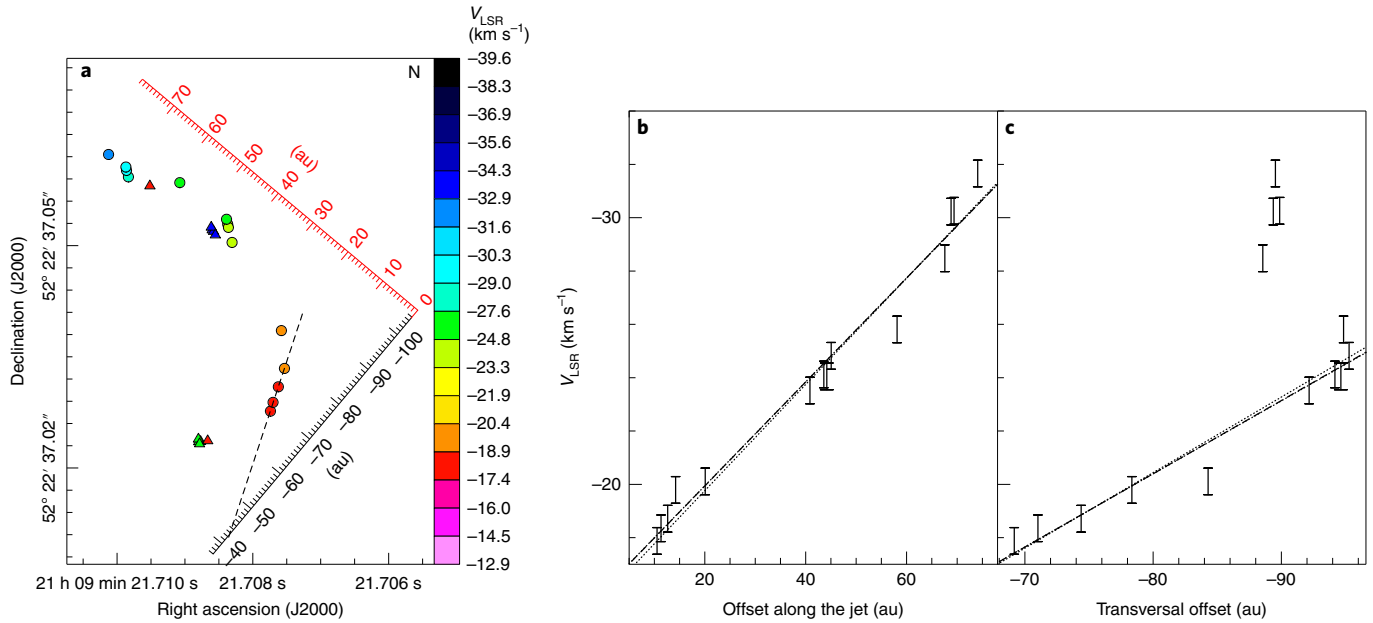

Fig. 6 | The co-rotating north stream. a, Expanding view of the maser positions and V_{LSR} in the north region. Coloured dots and triangles give absolute positions of the 22 GHz water masers, with colours denoting the maser V_{LSR}. The triangles mark a few masers with detached V_{LSR} excluded from the kinematical analysis. The distances along the jet (red) and disk (black) axes are indicated. The black dashed line shows the linear fit of the positions of the masers at elevation z < 20 au. **b**,**c**, Plot of maser V_{LSR} versus z (**b**) and R (**c**). In both panels, error bars denote the maser V_{LSR} and corresponding 2σ errors, and the black dashed and dotted lines show the best linear fit and the associated uncertainty, respectively. The linear fit of V_{LSR} versus R has been performed considering only the masers with V_{LSR} ≥ −27 km s^{-1}.

the derived streaming velocities are too small. First, comparing them with the values of V_{off} (Table 1), the two velocities have similar amplitudes, and this is inconsistent with the expectation that V_{off} is the line-of-sight component of V_z and that the jet axis is close to the plane of the sky. Second, taking the ratio between the highest elevations reached by the masers, that is 100–130 au (Figs. 4 and 5), and the above values of V_z, the derived travelling times of 15–40 yr exceed the separation of 10 yr since the previous VLBA

Table 2 | Estimate of the stream parameters

Stream	V_z (km s^{-1})	ω_K (km s^{-1} au^{-1})	$\mathfrak{R}_K$ (au)
SW	≥48	≥2.9	≤9
NE-1	≥46	≥2.6	≤10
NE-2	≥9	≥1.0	≤17
NE-3	≥85	≥5.4	≤6

Column 1 indicates the maser stream. Column 2 reports the estimated streaming velocity along the jet axis. Columns 3 and 4 give the estimate of the angular velocity and the radius, respectively, at the launch point.

observations, when no maser emission was detected at corresponding positions.

As V_{off} corresponds to the line-of-sight projection of V_z, we can write:

$$V_z = \| V_{off} - V_{sys} \| / \sin(i_{axi}) \quad (8)$$

where V_{off} is corrected for the systemic V_{LSR} of the YSO, and i_{axi} is the inclination angle of the jet axis with the plane of the sky. As we know that $i_{axi} \leq 30°$, equation (8) allows us to derive a lower limit for V_z, reported in Table 2. Using the derived lower limit of V_z and the corresponding value of f_z (Table 1), by means of equation (7) we can calculate a lower limit for ω_e. Finally, we use equation (6) and the fitted value of ω (Table 1) to infer a lower limit for $\omega_K = \omega + \|\omega_e\|$ and, knowing the mass of the YSO, a corresponding upper limit for the launch radius $\mathfrak{R}_K$ (Table 2). The NE-1 stream, which extends the most in elevation (from 20 au to 130 au; Fig. 5a), includes a group of maser features at elevation of ~20 au, which should be located closer to the Alfvén point. In 'Constraining the Alfvén point of the NE-1 stream' in Supplementary Information, we study the change of V_{LSR} versus R internal to this cluster and obtain a lower limit for $\omega_K \geq 2.4$ km s^{-1} au^{-1} that agrees well with the corresponding value reported in Table 2 for the NE-1 stream. The results shown in Table 2 are in general agreement with the theoretical predictions from MHD disk winds[18,19]: the inferred lower limits on the streaming velocity V_z increase steeply with decreasing launch radius; for the southwest and NE-3 streams, which are those with relatively lower uncertainty in the measurement of both ω and $\mathfrak{R}$ (Table 1), the ratio between V_z and the rotation velocity $\omega\,\mathfrak{R}$ is ≥2–3.

In conclusion, our observations resolve the kinematics of an MHD disk wind on length scales of 1–100 au, allowing us to study the velocity pattern of individual streamlines launched from the disk. As represented in Fig. 2b, close to the disk rotation axis, we observe flows spiralling outwards along a helical magnetic field, launched from locations of the disk at radii ≤6–17 au. At larger separation from the rotation axis, we observe a stream of gas co-rotating with its launch point from the disk at radius of ~40 au, in agreement with the predictions for magneto-centrifugal acceleration. Our interpretation is supported by (resistive-radiative-gravito-) MHD simulations of the formation of a massive star that lead to a magneto-centrifugally launched jet whose properties agree with our maser and thermal (continuum and line) observations of IRAS 21078+5211. These results provide a clear evidence for an MHD disk wind. As water maser emission is widespread in YSOs, sensitive VLBI observations of water masers can be a valuable tool to investigate the physics of disk winds.

Methods

Observations. We observed the 6_{16}–5_{23} H_2O maser transition (rest frequency 22.235079 GHz) towards IRAS 21078+5211 (tracking centre: right ascension (J2000) = 21 h 9 min 21.720 s and declination (J2000) = +52° 22′ 37.08″) with global VLBI for 24 h, starting on 27 October 2020 at 13:30 UT. The antennae involved were 16 antennae of the European VLBI network (EVN): Yebes, Sardinia, Medicina, Jodrell Bank, Effelsberg, Onsala, Metsahovi, Torun, Svetloe, Badary, Zelenchukskaya, KVN_Tamna, KVN_Ulsan, KVN_Yonsei, Urumqi and Tianma; plus the 10 antennae of the VLBA: Brewster, Fort Davis, Hancock, Kitt Peak, Los Alamos, Mauna Kea, North Liberty, Owens Valley, Pie Town and Saint Croix. The observations were designed to achieve a relative and absolute position accuracy of ~0.01 mas and ~1 mas, respectively, and to reach a sensitivity in the maser line ≤1 mJy per beam. While the EVN antennae observed continuously the target, interleaving calibration scans ~8 min long every hour, the VLBA performed also phase-referencing observations (over 10 h), alternating scans on the target and the phase-reference calibrator every 45 s. During the phase-reference session, the target and the calibrators were always observed by the VLBA simultaneously with the EVN to ensure global VLBI baselines. The fringe-finder and bandpass calibrators were: J2202+4216, 2007+777, 3C84 and 3C48; the phase-reference calibrators were 2116+543 and 2051+528, both within 2.5° from the target and with a correlated flux of ~0.1 Jy per beam at 22 GHz.

We recorded dual circular polarization through four adjacent bandwidths of 16 MHz, one of them centred at the maser V_{LSR} of −6.4 km s^{-1}. The four 16 MHz bandwidths were used to increase the signal-to-noise ratio (SNR) of the weak continuum (phase reference) calibrators. The data were correlated with the SFXC correlator at the Joint Institute for VLBI in Europe (JIVE, at Dwingeloo, the Netherlands) in two correlation passes, using 1,024 and 128 spectral channels to correlate the maser 16 MHz bandwidth and the whole set of four 16 MHz bandwidths, respectively. The spectral resolution attained across the maser 16 MHz band was 0.21 km s^{-1}. The correlator averaging time was 1 s.

Data were reduced with the Astronomical Image Processing System (AIPS) package following the VLBI spectral line procedures[24]. The emission of an intense and compact maser channel was self-calibrated, and the derived (amplitude and phase) corrections were applied to all the maser channels before imaging. To cover the whole maser emission, we produced images extending 0.65″ in both right ascension cosδ and declination, and 84 km s^{-1} in V_{LSR}. Using natural weighting, the full-width at half-maximum (FWHM) major and minor sizes of the beam are 0.7 mas and 0.3 mas, respectively, and the beam PA is −49°. In channel maps with (relatively) weak signal, the 1σ root-mean-square noise is 0.7 mJy per beam, close to the expected thermal noise.

Inverse phase-referencing[24] produced good SNR (≥10) images of the two phase-reference calibrators. Taking into account that the calibrators are relatively compact with size ≲1 mas, and that the absolute position of the calibrators is known within a few 0.1 mas, we estimate that the error on the absolute position of the masers is ≲0.5 mas.

Supplementary Table 1 reports the parameters (intensity, V_{LSR}, position) of the 22 GHz water masers in IRAS 21078+5211. Individual maser features are a collection of quasi-compact spots observed on contiguous channel maps and spatially overlapping (within their FWHM size). The spot positions are determined by fitting a 2D elliptical Gaussian to their spatial emissions. The uncertainty of the spot position relative to the reference maser channel is the contribution of two terms: $\Delta\theta_{spot} = \sqrt{\Delta\theta^2_{fit} + \Delta\theta^2_{bandpass}}$. The first term depends on the SNR of the data, following[25]: $\Delta\theta_{fit} = \theta_{beam}$ / (2 SNR), where θ_{beam} is the resolution beam size, conservatively taken equal to the FWHM major beam size of 0.7 mas. The second term depends on the accuracy of the bandpass calibration through the expression[26]: $\Delta\theta_{bandpass} = \theta_{beam}$ ($\Delta\Psi$/360°), where $\Delta\Psi$ in degrees is the phase stability across the observing band. In our case $\Delta\Psi \lesssim 10°$ and $\Delta\theta_{bandpass} \lesssim 0.02$ mas becomes the dominant error term for spot intensity ≥100 mJy per beam. The maser feature position (and corresponding error) is estimated from the error-weighted mean of the spot positions (and corresponding errors), and the feature V_{LSR} from the intensity-weighted mean of the spots' V_{LSR}. To be conservative, the uncertainty on the feature V_{LSR} is taken equal to 0.5 km s^{-1}, corresponding to the typical maser FWHM line width.

Velocity scatter. Figures 4b and 5b show that the maser V_{LSR} are linearly correlated with R in the southwest and NE-1 streams. For the masers belonging to the NE-2 stream, the measurement scatter from the linear fit of V_{LSR} versus R is considerable (with large fit errors; Table 1), while, in the case of the NE-3 stream, the range in R is too small (only 2 au) to constrain the parameters of the linear fit. The noticeable deviation of V_{LSR} from the linear fits seems difficult to conciliate with the accuracy with which the maser positions reproduce the sinusoidal patterns (Figs. 4c and 5c). The average scatters of maser V_{LSR} and positions (along the jet axis from the fitted sinusoid) are 2.4 km s^{-1} and 1.9 au, 3.1 km s^{-1} and 3.8 au, 6.9 km s^{-1} and 2.1 au, and 2.7 km s^{-1} and 1.7 au, for the southwest, NE-1, NE-2 and NE-3 streams, respectively. Assuming that the V_{LSR} scatter reflects mainly the variation of the streaming velocity V_z, since the jet axis is within 30° from the plane of the sky, the change in V_z has to be at least twice that observed in V_{LSR}. Then, using the above values, the ratios of the corresponding scatters in position and V_z give upper limits for the maser travelling times of ≤1–3 yr. These travelling times, for maximum (absolute) elevations of the maser streams of 100–130 au (Figs. 4 and 5), imply $V_z \geq 200$–500 km s^{-1}, which appears to be too large with respect to the observed maser V_{LSR}. In the following, we investigate the physical reason for the observation of well-defined sinusoidal patterns despite the co-occurrence of significant velocity scatters.

In a stationary, axisymmetric MHD flow, the two fundamental equations of motions[18,19,27] linking velocity and magnetic field along a field line are:

$$\rho V_{\rm p} = kB_{\rm p} \tag{9}$$

$$B_\phi = \frac{\rho}{k}\,(V_\phi - \omega_{\rm K}\mathfrak{R}) \tag{10}$$

where $V_{\rm p}$ and V_ϕ, and $B_{\rm p}$ and B_ϕ are the poloidal and toroidal components of the velocity and magnetic field, respectively, ρ is the gas mass volume density, $\omega_{\rm K}$ is the Keplerian angular velocity at the launch point, $\mathfrak{R}$ is the rotation radius and k is the 'mass load' of the wind, expressing the fixed ratio of mass and magnetic fluxes along a given magnetic-field line. As $V_\phi - \omega_{\rm K}\,\mathfrak{R}$ is the toroidal velocity in the reference frame co-rotating with the launch point, equations (9) and (10) lead to the well-known result that the velocity and magnetic-field vectors are always parallel in the co-rotating reference frame. Writing $V_\phi = \omega\,\mathfrak{R}$, where ω is the angular velocity of the trajectory at radius $\mathfrak{R}$, the two equations above can be combined into:

$$\frac{B_\phi}{B_{\rm p}} = \frac{(\omega - \omega_{\rm K})}{V_{\rm p}}\,\mathfrak{R} = \frac{\omega_{\rm e}}{V_{\rm p}}\,\mathfrak{R} \tag{11}$$

where we have used the definition of $\omega_{\rm e}$ in equation (6). We can define the magnetic-field helix angle $\alpha_B = \arctan(B_\phi/B_{\rm p})$, which is the angle with which a helical field line winds around the jet axis.

We have seen that the observation of well-defined sinusoids in the plane of the sky requires that the rotation radius $\mathfrak{R}$, and the ratio of the effective angular velocity $\omega_{\rm e}$ on the streaming velocity V_z keep constant (equation (7)). As the poloidal velocity $V_{\rm p}$ is equal to V_z if $\mathfrak{R}$ is constant, equation (11) implies that α_B does not vary along each of the observed maser streams. However, the reverse argument holds too. If the magnetic field is sufficiently stable and has a constant helix angle (that is, a helical configuration), the motion along the field line (in the co-rotating reference frame) requires a constant value of the ratio $\omega_{\rm e}/V_z$. This preserves the maser sinusoidal pattern despite the concomitant presence of a relatively large velocity scatter. From equations (11) and (7), with $V_{\rm p} = V_z$, we have:

$$\frac{\parallel B_\phi \parallel}{B_{\rm p}} = f_z\,\mathfrak{R} \tag{12}$$

Using the values reported in Table 1, we derive: $f_z\,\mathfrak{R} = 0.79 \pm 0.06$, 1.1 ± 0.2, 0.88 ± 0.04 and 0.70 ± 0.05 for the southwest, NE-1, NE-2 and NE-3 streams, respectively. From equation (10), $B_\phi \approx 0$ within the Alfvén point when the flow co-rotates with the disk and $V_\phi \approx \omega_{\rm K}\,\mathfrak{R}$. Beyond the Alfvén point, the inertia of the matter in the flow forces the magnetic field to fall behind the rotation of the disk, which causes $\|B_\phi\|$ to increase. The derived values of the ratio $\|B_\phi\|/B_{\rm p}$ in the range 0.7–1.1 agree with the water masers tracing a region of the spiralling trajectory in between the Alfvén point and the fast magneto-sonic point, beyond which the toroidal magnetic-field component should become the predominant component[18,28].

Finally, we discuss briefly possible causes for the observed velocity scatter. For the southwest, NE-1 and NE-2 spiral motions, the residual of the linear fit of $V_{\rm LSR}$ versus R is plotted versus z in Supplementary Fig. 2. These plots indicate that the residual velocity is not correlated with position, contrarily to what it would be expected if the velocity scatter from the linear fit was caused by the smooth change with z of the characteristic velocities, ω and V_z (and consequently $V_{\rm off}$), of the spiralling trajectory. The residual velocities cannot be dominated by turbulence, too, as the latter would produce an independent variation of the toroidal and poloidal velocity components, which, as discussed above, is not consistent with the observation of the maser sinusoidal patterns. Moreover, it would be difficult to explain the observed different degree of turbulence between the NE-1 and NE-2 streams (Supplementary Fig. 2) over the same region of the sky.

The irregular change of the velocities can be naturally linked to our flow tracers, the water masers, which are excited in internal shocks of the flow emerging from perturbed locations of the disk. Equations (9) and (10) show that the flow velocity depends critically on the mass load k, which, in turn, depends on the physical conditions, including dissipative processes, near the disk surface. If the physical conditions of the perturbed launch points varied erratically on timescales as short as months, that would qualitatively explain the observed scatter of maser velocities. Emission variability over timescales of months is observed and theoretically expected in accretion bursts from high-mass YSOs[29–31], in such cases where an extended portion of the accretion disk gets perturbed.

Shock type and corresponding flow kinematics of water masers. We propose that the water masers observed in IRAS 21078+5211 inside the northeast, southwest and north regions arise in internal shocks along streamlines of the YSO's disk wind. If observed at sufficiently high angular resolution, radio jets are often resolved into chains of compact emission centres (named 'knots'), which are interpreted in terms of internal shocks owing to fluctuation in mass or velocity ejection[32]. As the jets are the innermost (most collimated and fastest) portion of a disk wind, it is possible that the structure of more external streamlines, where the gas is weakly ionized and mainly molecular, is characterized by internal shocks, too. If the fluctuation responsible for the shocks is relatively small compared with the (time average) flow properties, the internal shocks are weak C-shocks and the shock (and maser) velocity is close to the flow velocity. In fact, the proper motions of radio knots are considered a reliable measurement of the jet speed[32]. In IRAS 21078+5211, the regular (arc-like) spatial and $V_{\rm LSR}$ distribution of the water masers indicate that the masers co-move with the flowing gas.

Models of water maser excitation predict them to arise in both strong dissociative J-shocks[21,33] and weak non-dissociative C-shocks[22]. While in J-shocks the masers form in the cooling post-shock gas at kinetic temperature $T_{\rm kin} \approx 400$ K following the chemical re-formation of water, in C-shocks the masing molecules do not dissociate and reach a significantly higher temperature, $T_{\rm kin} \approx 1{,}000{-}3{,}000$ K. The presence of shocks is naturally expected in correspondence with the fast protostellar outflows, whose association with the 22 GHz water masers is well proved observationally[34]. The location of the 22 GHz masers, often found at the wall of the jet cavity or at the terminal bow shock of the jet, and their speed (mainly $\lesssim 30$ km s^{-1})[17] significantly smaller that that of the jet (a few 100 km s^{-1})[32], indicate that the large majority of the 22 GHz water masers arise in strong external (lateral or terminal) J-shocks of the fast flow against the dense ambient material. While the velocity of the internal shocks is close to the flow speed, external shocks travel at a reduced speed because of the density contrast between the lighter impinging flow and the denser surrounding material.

As exemplified by our observations in IRAS 21078+5211, the origin of the 22 GHz masers in internal shocks of the flow make them a formidable tool to trace individual streams of gas of the disk wind. In the following, we show that the alternative interpretation for these masers as external shocks of a wide-angle wind or a jet impacting against the surrounding medium is much less plausible. Looking at Fig. 2a, the water masers could be found at the wall of a wind cavity if the axis of this putative wind was oriented at PA ≈ 10–$20°$ and its opening angle was ~30–40°. It is very difficult to conciliate this wide-angle wind with the jet geometry and precession rate estimated from previous (2010–2013) JVLA and VLBA observations (Fig. 1). The elongation (PA $= 56 \pm 12°$) of the slightly resolved (size ~150 au) JVLA continuum at 1.3 cm, the collimated (PA $= 49 \pm 18°$) proper motions of the water masers near (100–200 au) the YSO, and the direction (PA $\approx 44°$) of the non-thermal radio jet traced by the extended (size ~1,000 au) JVLA continuum at 5 cm consistently indicate the presence of a jet oriented at PA $\approx 50°$. A distinct signature of precession[17] was the finding of a spur in the 5 cm continuum ~7,000 au northeast from the YSO along the same direction, PA $= 60°$, of the redshifted lobe of the outflow observed in sulfur monoxide (SO) emission with NOEMA. Clearly, a precession rate of only $\sim(60° - 50°) = 10°$ over a length scale of 7,000 au cannot account for a change in orientation between the putative wind and the JVLA/VLBA jet of $\geq(50° - 20°) = 30°$ over a length scale $\leq$100 au and a timescale $\leq$10 yr. However, if this inner wind and the jet co-existed, it would be even more difficult to explain an abrupt transition in orientation and opening angle from the former to the latter across a few 10 au (Fig. 2a). The interpretation of the water masers in IRAS 21078+5211 as external shocks at the cavity wall of a wide-angle wind faces also the difficulty to account for the huge maser $V_{\rm LSR}$ gradients, ≥ 40 km s^{-1} over $\leq$10 au, transversal to the northeast stream at elevation $z \geq 90$ au (Fig. 5a). If the masers, instead of delineating two streams at different velocities, traced shock fronts (seen close to edge-on) at the wind wall, it would be very difficult to explain such a large velocity difference for almost overlapping emissions.

We conclude this discussion on alternatives to the disk-wind interpretation showing that it is improbable that we are observing multiple outflows from a binary system. Inspecting Fig. 1, our previous NOEMA, JVLA and VLBA observations consistently indicate a single disk–jet system on scales of 100–500 au. The NOEMA 1.37 mm and the JVLA 1.3 cm continuum emissions, tracing the hosting molecular core and YSO's activity, respectively, are compact and well aligned in position. The rotating disk revealed by the $V_{\rm LSR}$ gradient of high-density molecular (CH_3CN and HC_3N) lines is centred on the peak of the 1.3 cm continuum. The agreement in direction between the elongated (double lobe) JVLA 5 cm continuum and the collimated water maser proper motions points to a single jet emerging from the YSO. Considering now the new, global VLBI observations, on scales of 1–100 au, Fig. 2a shows that the spatial distribution of the water masers is about symmetrical with respect to the YSO position. This further supports the interpretation that a single YSO is responsible for the excitation and motion of the water masers.

Kinematics of the water masers further to northeast and south. In the main text, we have considered only the filaments of maser emission inside the northeast, southwest and north regions, but more scattered maser features are also observed further to northeast close to the jet axis and south of the YSO (Fig. 2a). The outmost northeastern features are found approximately in the same region of the previous VLBA maser detections (Fig. 2a). However the newly observed masers are fewer than before and their $V_{\rm LSR}$ is now within ± 5 km s^{-1} from $V_{\rm sys}$ instead of covering the range $[-38, 0]$ km s^{-1} as before. The directions of the VLBA maser proper motions are well collimated but their amplitudes (in the range $[10, 50]$ km s^{-1}) scatter significantly in position (Fig. 1b), which, as discussed in 'Shock type and corresponding flow kinematics of water masers', suggests that these masers arise in external shocks and do not trace the true flow speed. In

our previous analysis[17], we have interpreted these outmost northeastern masers as external shocks at the wall of a cylindrical MHD jet interacting with the surrounding medium. Applying the equations for an MHD disk wind, we have derived a terminal jet speed of ~200 km s^{-1} and a launch radius of ~2 au. These values agree with the trend of the calculations reported in Table 2, where higher streaming velocities correspond to smaller launch radii.

The southern features are distributed in three separated clusters (Fig. 2a): C1, $z \lesssim 20$ au and 9.5 km s$^{-1} \leq V_{LSR} \leq 17.4$ km s^{-1}; C2, 20 au $\lesssim z \lesssim 100$ au and 5.5 km s$^{-1} \leq V_{LSR} \leq 9.5$ km s^{-1}; C3, $z \gtrsim 120$ au and 5.5 km s$^{-1} \leq V_{LSR} \leq 29.7$ km s^{-1}. Comparing the C1 and C2 clusters with the north region, maser positions and V_{LSR} are about symmetrical with respect to the YSO; besides, each of the two clusters presents an arc-like shape similar to the north streamline. Thus, it is possible that these clusters trace small portions of two co-rotating streamlines emerging at different disk radii. Finally, the maser cluster C3 has position and V_{LSR} approximately symmetrical to the emission previously observed with the VLBA further to northeast (Fig. 1b), which suggests that masers in C3 can emerge in shocks at the wall of the southeastern lobe of the jet.

Simulation snapshot of a forming massive star. As part of a more extensive study we will describe in a forthcoming article, we performed an axisymmetrical simulation of the formation of a massive star starting from the gravitational collapse of a rotating cloud core threaded by a magnetic field (A.O. and R.K., submitted). We used the methods of magnetohydrodynamics to model the weakly ionized gas and dust with the code Pluto[35], with an ohmic resistivity model as a non-ideal effect[36], and additional modules for self-gravity[37] and the transport of the thermal radiation emitted by the gas and dust[38].

The cloud core has an initial mass of 100 $M_\odot$ and a radius of 0.1 pc. The assumed conditions for the onset of the gravitational collapse ($t=0$) are as follows: the density is distributed according to $\rho \propto r^{-1.5}$, the cloud core rotates like a solid body with a rotational energy equivalent to 4% of its gravitational energy content, and the magnetic field is uniform. The initial magnitude of the magnetic field is determined by the mass-to-flux ratio, which we take as 20 times the critical (collapse preventing) value[39] and corresponds to a relatively weak initial magnetic field. A constant value of the opacity of 1 cm^2 g^{-1} was used to model the gas and dust, as well as an initial dust-to-gas mass ratio of 1%.

We used an axisymmetrical grid of 896 × 160 cells in spherical coordinates, with the radial coordinate increasing logarithmically with the distance to the centre of the cloud. An inner boundary of 3 au was set up, inside of which the protostar is formed through accretion. No flows are artificially injected from the inner boundary into the collapsing cloud.

The simulation starts with an initial gravitational collapse epoch. After ~5 kyr, enough angular momentum is transported to the centre of the cloud to start forming an accretion disk that grows in size over time. Roughly at the same time, we observe the launch of magnetically driven outflows. Magnetic pressure arising from the dragging of magnetic-field lines by the rotating flow eventually overcomes gravity and seeds the formation of the outflow cavity, thrusting a bow shock in the process (Supplementary Fig. 1d), which propagates outwards as the cavity grows in size. Previous observations of IRAS 21078+5211 have uncovered the presence of a bow shock located at distances of ~36,000 au from the forming massive YSO[17]. The initial launch of the magnetically driven outflows provides a possible formation mechanism for the observed bow shock and in return, the propagation of the bow shock provides an estimation for the age of the system.

In the simulation, the protostar reaches a mass of 5.24 $M_\odot$ (a value in the expected mass interval from observations) after 13.84 kyr of evolution. We estimate that the bow shock has propagated to a distance of ~30,000 au at that time, roughly in line with the observations. At the same time, the accretion disk has grown to about 180 au in radius, in agreement with the observational estimates[17], as well. The data reveal a magneto-centrifugally launched jet, in a similar way as reported by the literature[2,40]; however, we see that the launching region of the jet is narrowed by the ram pressure of the infalling material from the envelope and the presence of a thick layer of the accretion disk that is vertically supported by magnetic pressure. Material transported from large scales through the accretion disk reaches the launching region, located at $z \lesssim 100$ au (Supplementary Fig. 1b), where the centrifugal force is stronger than gravity, and simultaneously, where the flow becomes sub-Alfvénic in the co-rotating frame and the magnetic-field lines are mostly poloidal. Under these conditions, a parcel of plasma is accelerated along the field lines until the flow becomes super-Alfvénic again, a point at which the magnetic-field lines become mostly toroidal. This causes the parcel to acquire a helical trajectory (depicted previously in Fig. 2b). The geometry and kinematics of the region where the flow becomes helical in the simulation coincides roughly with the positions and velocities of the observed masers of the northeast and southwest regions. At larger rotation radii, the broader magnetic-field lines present in the outflow cavity could give rise to the kinematic footprint detected in the masers in the north region.

At distances of ~10,000 au, where the outflow material propagates through the cloud (Supplementary Fig. 1c), we notice the existence of re-collimation zones that arise because of magnetic hoop stress and ram pressure from the envelope. The position of the re-collimation zones is similar to the zones where lobes of possible synchrotron emission have been previously observed around the YSO[17], thus providing a possible mechanism for their formation.

We provide this comparison as an example that a magneto-centrifugally launched jet around a forming massive star yields a consistent picture with the observations. However, the coincidences should be taken with caution, as different combinations of initial conditions may yield similar results, which means that a wider and deeper investigation is needed to determine the conditions of the onset of star formation from the observational data.

Data availability

This article makes use of the following EVN data: GM077 (EVN project code). The calibrated datasets generated during and/or analysed during the current study are available from the corresponding author on reasonable request.

Code availability

The custom parts of the code for producing the simulations and subsequent data analysis are not ready for public use, but they can be provided upon reasonable request. For the magnetohydrodynamics part of the software, we make use of the open-source code Pluto[35,41]. The implementation method of the employed radiation transport module ('Makemake') is publicly accessible[38].

Received: 8 June 2022; Accepted: 4 July 2022;
Published online: 11 August 2022

References

1. Pudritz, R. E. & Norman, C. A. Centrifugally driven winds from contracting molecular disks. *Astrophys. J.* **274**, 677–697 (1983).
2. Blandford, R. D. & Payne, D. G. Hydromagnetic flows from accretion disks and the production of radio jets. *Mon. Not. R. Astron. Soc.* **199**, 883–903 (1982).
3. Ouyed, R. & Pudritz, R. E. Numerical simulations of astrophysical jets from Keplerian Disks. I. Stationary models. *Astrophys. J.* **482**, 712–732 (1997).
4. Krasnopolsky, R., Li, Z.-Y. & Blandford, R. Magnetocentrifugal launching of jets from accretion disks. I. Cold axisymmetric flows. *Astrophys. J.* **526**, 631–642 (1999).
5. Bacciotti, F., Ray, T. P., Mundt, R., Eislöffel, J. & Solf, J. Hubble Space Telescope/STIS spectroscopy of the optical outflow from DG Tauri: indications for rotation in the initial jet channel. *Astrophys. J.* **576**, 222–231 (2002).
6. Hirota, T. et al. Disk-driven rotating bipolar outflow in Orion Source I. *Nat. Astron.* **1**, 0146 (2017).
7. Lee, C.-F. et al. A rotating protostellar jet launched from the innermost disk of HH 212. *Nat. Astron.* **1**, 0152 (2017).
8. Aalto, S. et al. ALMA resolves the remarkable molecular jet and rotating wind in the extremely radio-quiet galaxy NGC 1377. *Astron. Astrophys.* **640**, A104 (2020).
9. Tabone, B. et al. Constraining MHD disk winds with ALMA. Apparent rotation signatures and application to HH212. *Astron. Astrophys.* **640**, A82 (2020).
10. Matthews, L. D. et al. A feature movie of SiO emission 20–100 au from the massive young stellar object Orion Source I. *Astrophys. J.* **708**, 80–92 (2010).
11. Moscadelli, L. & Goddi, C. A multiple system of high-mass YSOs surrounded by disks in NGC 7538 IRS1. Gas dynamics on scales of 10–700 au from CH_3OH maser and NH_3 thermal lines. *Astron. Astrophys.* **566**, A150 (2014).
12. Sanna, A. et al. Velocity and magnetic fields within 1000 au of a massive YSO. *Astron. Astrophys.* **583**, L3 (2015).
13. Moscadelli, L., Cesaroni, R., Rioja, M. J., Dodson, R. & Reid, M. J. Methanol and water masers in IRAS 20126+4104: the distance, the disk, and the jet. *Astron. Astrophys.* **526**, A66 (2011).
14. Burns, R. A. et al. A 'water spout' maser jet in S235AB-MIR. *Mon. Not. R. Astron. Soc.* **453**, 3163–3173 (2015).
15. Moscadelli, L. et al. Outflow structure within 1000 au of high-mass YSOs. I. First results from a combined study of maser and radio continuum emission. *Astron. Astrophys.* **585**, A71 (2016).
16. Xu, Y. et al. On the nature of the local spiral arm of the Milky Way. *Astrophys. J.* **769**, 15 (2013).
17. Moscadelli, L. et al. Multi-scale view of star formation in IRAS 21078+5211: from clump fragmentation to disk wind. *Astron. Astrophys.* **647**, A114 (2021).
18. Pudritz, R. E., Ouyed, R., Fendt, C. & Brandenburg, A. in *Disk Winds, Jets, and Outflows: Theoretical and Computational Foundations. Protostars and Planets V* (eds Reipurth, B. et al.) 277-294 (2007), University of Arizona Press, Tucson.
19. Pudritz, R. E. & Ray, T. P. The role of magnetic fields in protostellar outflows and star formation. *Front. Astron. Space Sci.* **6**, 54 (2019).
20. Elitzur, M., Hollenbach, D. J. & McKee, C. F. Planar H_2O masers in star-forming regions. *Astrophys. J.* **394**, 221–227 (1992).
21. Hollenbach, D., Elitzur, M. & McKee, C. F. Interstellar H_2O masers from J shocks. *Astrophys. J.* **773**, 70 (2013).
22. Kaufman, M. J. & Neufeld, D. A. Water maser emission from magnetohydrodynamic shock waves. *Astrophys. J.* **456**, 250–+ (1996).
23. Pesenti, N. et al. Predicted rotation signatures in MHD disc winds and comparison to DG Tau observations. *Astron. Astrophys.* **416**, L9–L12 (2004).

24. Sanna, A. et al. VLBI study of maser kinematics in high-mass star-forming regions. I. G16.59−0.05. *Astron. Astrophys.* **517**, A71 (2010).
25. Reid, M. J. et al. The distance to the center of the galaxy—H_2O maser proper motions in Sagittarius B2(N). *Astrophys. J.* **330**, 809–816 (1988).
26. Zhang, Q., Claus, B., Watson, L. & Moran, J. Angular momentum in disk wind revealed in the young star MWC 349A. *Astrophys. J.* **837**, 53 (2017).
27. Pelletier, G. & Pudritz, R. E. Hydromagnetic disk winds in young stellar objects and active galactic nuclei. *Astrophys. J.* **394**, 117 (1992).
28. Staff, J., Koning, N., Ouyed, R. & Pudritz, R. Three-dimensional simulations of MHD disk winds to hundred AU scale from the protostar. Eur. *Phys. J. Web Conf* **64**, 05006 (2014).
29. Caratti o Garatti, A. et al. Disk-mediated accretion burst in a high-mass young stellar object. *Nat. Phys.* **13**, 276–279 (2017).
30. Hunter, T. R. et al. An extraordinary outburst in the massive protostellar system NGC 6334I−MM1: quadrupling of the millimeter continuum. *Astrophys. J. Lett.* **837**, L29 (2017).
31. Oliva, G. A. & Kuiper, R. Modeling disk fragmentation and multiplicity in massive star formation. *Astron. Astrophys.* **644**, A41 (2020).
32. Anglada, G., Rodríguez, L. F. & Carrasco-González, C. Radio jets from young stellar objects. *Astron. Astrophys. Rev.* **26**, 3 (2018).
33. Elitzur, M., Hollenbach, D. J. & McKee, C. F. H_2O masers in star-forming regions. *Astrophys. J.* **346**, 983–990 (1989).
34. Moscadelli, L. et al. Protostellar Outflows at the Earliest Stages (POETS). IV. Statistical properties of the 22 GHz H_2O masers. *Astron. Astrophys.* **635**, A118 (2020).
35. Mignone, A. et al. PLUTO: a numerical code for computational astrophysics. *Astrophys. J. Suppl. Ser.* **170**, 228–242 (2007).
36. Machida, M. N., Inutsuka, S.-i & Matsumoto, T. Magnetic fields and rotations of protostars. *Astrophys. J.* **670**, 1198–1213 (2007).
37. Kuiper, R., Klahr, H., Beuther, H. & Henning, T. Circumventing the radiation pressure barrier in the formation of massive stars via disk accretion. *Astrophys. J.* **722**, 1556–1576 (2010).
38. Kuiper, R., Yorke, H. W. & Mignone, A. Makemake + Sedna: a continuum radiation transport and photoionization framework for astrophysical newtonian fluid dynamics. *Astrophys. J. Suppl. Ser.* **250**, 13 (2020).
39. Mouschovias, T. C. & Spitzer, J. L. Note on the collapse of magnetic interstellar clouds. *Astrophys. J.* **210**, 326 (1976).
40. Kölligan, A. & Kuiper, R. Jets and outflows of massive protostars. From cloud collapse to jet launching and cloud dispersal. *Astron. Astrophys.* **620**, A182 (2018).
41. Mignone, A. et al. PLUTO: a code for flows in multiple spatial dimensions. *Astrophysics Source Code Library* ascl:1010.045 (2010).

Acknowledgements

We thank C. Fendt and D. Galli for useful discussion. A.O. acknowledges financial support from the Deutscher Akademischer Austauschdienst (DAAD), under the programme Research Grants - Doctoral Projects in Germany, and complementary financial support for the completion of the doctoral degree by the University of Costa Rica, as part of their scholarship programme for postgraduate studies in foreign institutions. H.B. acknowledges support from the European Research Council under the Horizon 2020 Framework Programme via the ERC Consolidator Grant CSF-648505. H.B. also acknowledges support from the Deutsche Forschungsgemeinschaft in the Collaborative Research Center (SFB 881) 'The Milky Way System' (subproject B1). R.K. acknowledges financial support via the Emmy Noether and Heisenberg Research Grants funded by the German Research Foundation (DFG) under grant numbers KU 2849/3 and 2849/9. The European VLBI Network is a joint facility of independent European, African, Asian and North American radio astronomy institutes. Scientific results from data presented in this publication are derived from the following EVN project code: GM077.

Author contributions

L.M. led the project, analysis, discussion and drafted the manuscript. A.S., H.B. and R.K. commented on the manuscript and participated in the discussion. A.O. and R.K. performed the numerical jet simulations described in 'Simulation snapshot of a forming massive star' in Methods. A.O. performed the dynamical analysis of the simulations, compared the simulation results to the observations, and produced the illustrations of the magnetic-field lines and streamlines.

Competing interests

The authors declare no competing interests.

Additional information

Supplementary information The online version contains supplementary material available at https://doi.org/10.1038/s41550-022-01754-4.

Correspondence and requests for materials should be addressed to Luca Moscadelli.

Peer review information *Nature Astronomy* thanks the anonymous reviewers for their contribution to the peer review of this work

Reprints and permissions information is available at www.nature.com/reprints.

Publisher's note Springer Nature remains neutral with regard to jurisdictional claims in published maps and institutional affiliations.